

# Theory of strained quantum emitters

Vytautas Žalandauskas,<sup>1,\*</sup> Rokas Silkinis,<sup>2</sup> Lukas Razinkovas,<sup>2</sup> Ali Tayefeh Younesi,<sup>3</sup> Minh Tuan Luu,<sup>3</sup> Ronald Ulbricht,<sup>3</sup> Ulrike Grossner,<sup>4</sup> Lasse Vines,<sup>1</sup> and Marianne Etzelmüller Bathen<sup>1,4,†</sup>

<sup>1</sup>*Department of Physics/Centre for Materials Science and Nanotechnology, University of Oslo, 0316 Oslo, Norway*

<sup>2</sup>*Department of Fundamental Research, Center for Physical Sciences and Technology (FTMC), Vilnius LT-10257, Lithuania*

<sup>3</sup>*Max-Planck Institut für Polymerforschung, Ackermannweg 10, 55128 Mainz, Germany*

<sup>4</sup>*Advanced Power Semiconductor Laboratory, ETH Zürich, Physikstrasse 3, 8092 Zürich, Switzerland*

(Dated: February 24, 2026)

Defects in semiconductors acting as optically active spin qubits are intriguing objects of fundamental study and future technological developments. These defect-based color centers are of particular interest for detection and response to physical variations such as pressure and strain. To investigate the defect emission response to strain, we have studied the vibrational structure of the negatively charged silicon vacancy ( $V_{\text{Si}}^-$ ) in 4H-SiC under applied tensile and compressive uniaxial strain using first-principles calculations. The strain variations of the emission spectrum can be explained by differing responses of bulk-like and quasi-localized vibrational modes. In particular, substantial differences are found between the hexagonal ( $h$ ) and quasicubic ( $k$ ) configurations of  $V_{\text{Si}}^-$  in 4H-SiC that result in a strain-induced improvement of the Debye–Waller factor for  $V_{\text{Si}}^-(h)$  under +2% uniaxial strain along the  $a$ -axis of 4H-SiC. Finally, strain-dependent changes in the phonon sideband enable distinguishing between compressive and tensile strain, opening up the possibility of magnetic field-free strain detection using only spin-conserving transitions of solid-state quantum emitters.

## I. INTRODUCTION

Defects in solids, such as color centers, are highly sensitive to their local environment, a property that underpins their broad use in quantum sensing applications [1, 2]. External perturbations alter the electronic and spin degrees of freedom of these defects, leading to distinct changes in their optical properties that facilitate the detection of temperature, pressure, or electromagnetic fields [3–10]. Among these perturbations, strain plays a unique role, as it directly alters the local crystal field and lattice dynamics, thereby affecting both optical transition energies and electron–phonon interactions. These effects are observed as measurable shifts and intensity redistributions in the zero-phonon line (ZPL) and the phonon sideband (PSB) of defect emission. Recent advances in first-principles optical lineshape calculations now enable a quantitative description of color center spectral properties, allowing defect identification and characterization through the detailed vibrational fingerprints present in the PSB [11–16]. However, a detailed microscopic understanding of defect–lattice interactions, with an emphasis on strain, that incorporates the intrinsic vibrational properties of solid-state color centers, is not yet available.

Among solid-state color centers, the nitrogen-vacancy (NV) center in diamond remains the most extensively studied and widely used system for quantum sensing applications [17]. Beyond diamond, silicon carbide (SiC) has emerged as an alternative platform, hosting a plethora of color centers with properties comparable

to those of the NV center and exhibiting environment-dependent spin and optical responses relevant for quantum sensing. In particular, emission from the silicon vacancy ( $V_{\text{Si}}$ ) [18] and divacancy ( $V_{\text{Si}}V_{\text{C}}$ ) defects [19] in 4H-SiC has been shown to respond to electric fields through a measurable Stark effect [20–24], while a pronounced strain response has been demonstrated for  $V_{\text{Si}}$  in 6H-SiC microparticles [25]. A quantitative understanding of strain-induced spectral shifts is essential for utilizing these defects as local pressure or stress gauges and for determining whether controlled strain can be employed to tailor and enhance their optical properties. The 4H-SiC polytype hosts well-characterized color centers which are sensitive to external perturbations [26], making it an ideal platform for probing the interplay between electronic structure, vibrational structure, and external pressure or strain. Previous work [22] investigated the strain dependence of emission from the  $V_{\text{Si}}$  in 4H-SiC but did not consider strain-induced modifications of the vibrational structure. We therefore consider the negatively charged silicon vacancy ( $V_{\text{Si}}^-$ ) in 4H-SiC as a test case for developing a comprehensive theoretical framework for strained solid-state color centers.

In this work, we present emission lineshapes calculated using state-of-the-art methodology for  $V_{\text{Si}}^-$  under tensile and compressive uniaxial strains applied along the  $a$ -axis of 4H-SiC, and compare these results with experimental emission spectra at zero strain. The electron–phonon interactions giving rise to the broad PSB are suggested as a potential readout mechanism capable of distinguishing between tensile and compressive strain. Furthermore, we predict that the  $V_{\text{Si}}^-(h)$  defect exhibits an enhanced Debye–Waller factor under +2% uniaxial strain relative to the strain-free case, demonstrating that strain, or other external perturbations, can be employed as a prac-

\* vytautas.zalandauskas@fys.uio.no

† m.e.bathen@fys.uio.no

tical tool to improve the properties of quantum emitters.

## II. METHODS

### A. First-principles calculations

The defect states were studied using density functional theory (DFT) calculations within the Kohn–Sham (KS) formalism. Computations were performed using the Vienna *ab initio* Simulation Package (VASP) [27–29]. The projector augmented-wave (PAW) method [30, 31] and plane waves were used to describe core and valence electrons, respectively. We utilized the meta-GGA class  $r^2$ SCAN functional [32]. This functional was selected for its capability in accurately capturing the structural, electronic, and vibrational properties of deep-level defects in 4H-SiC [33, 34]. Hexagonal 4H-SiC supercells containing either 576 or 400 atoms were constructed by repeating the primitive cell  $6 \times 6 \times 2$  times (zero strain) or  $5 \times 5 \times 2$  times (with strain) along the crystallographic axes. All calculations employed  $\Gamma$ -point sampling of the Brillouin zone and a plane-wave cutoff energy of 600 eV. The electronic self-consistent field (SCF) cycle and atomic forces were converged to within  $10^{-8}$  eV and  $5 \text{ meV \AA}^{-1}$ , respectively. Defects were created by removing a silicon atom from the lattice to form a silicon vacancy ( $V_{\text{Si}}$ ). Calculations were performed on the negative charge state of the  $V_{\text{Si}}$  ( $V_{\text{Si}}^-$ ) which is the only known optically bright state of this defect center.

### B. Vibrational structure calculations

Phonon modes for both bulk and defect supercells were calculated using the finite displacement method with configurations generated using the PHONOPY package [35]. Vibrational modes were extrapolated to the dilute limit using the embedding methodology of Refs. [11, 36], with further details provided in the Supplemental Material Sec. S3.

### C. Experimental setup

To measure the emission spectra at zero strain, we employ transient absorption spectroscopy [37] on a  $c$ -cut 4H-SiC substrate containing ensembles of  $V_{\text{Si}}$  [37, 38]. In contrast to traditional luminescence methods, where *spontaneous* emission is measured, we here measure the *stimulated* emission. See the Supplemental Material Sec. S5 for additional details and Ref. [39].

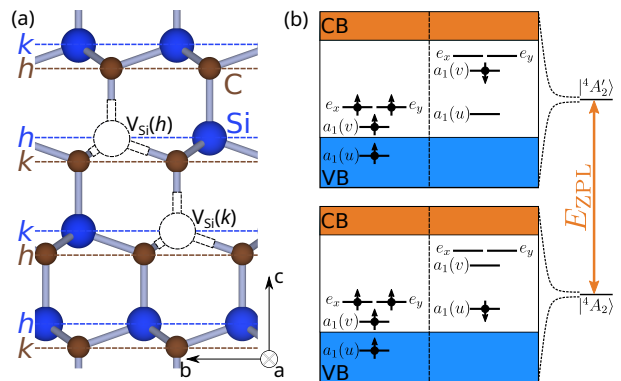


FIG. 1. (a) Ball-and-stick representation of the silicon vacancy ( $V_{\text{Si}}$ ) defect in 4H-SiC. Silicon and carbon atoms are shown as blue and brown spheres, respectively, while the vacancy site is depicted as a hollow sphere. Two nonequivalent configurations, hexagonal  $V_{\text{Si}}(h)$  and quasicubic  $V_{\text{Si}}(k)$ , are illustrated. The planes labeled  $h$  and  $k$  indicate the symmetry of the corresponding lattice sites. (b) Schematic representation of single-particle defect levels in the band gap of 4H-SiC showing their occupations in the ground  ${}^4A_2$  state (bottom) and excited  ${}^4A_2'$  state (top) of  $V_{\text{Si}}^-$ . The spin-majority channel (left side) is denoted with upward arrows and the spin-minority channel (right side) with downward arrows. Shaded areas correspond to the valence band (VB) in blue and the conduction band (CB) in orange.

## III. RESULTS AND DISCUSSION

### A. Electronic properties

In the 4H-SiC polytype, the Si–C bilayers stack along the crystallographic  $c$ -axis ([0001] direction), where each atomic site can adopt either a hexagonal ( $h$ ) or quasicubic ( $k$ ) configuration. Consequently, two nonequivalent configurations of the silicon vacancy,  $V_{\text{Si}}(h)$  and  $V_{\text{Si}}(k)$ , must be considered [see Fig. 1(a)]. The  $V_{\text{Si}}^-$  has a spin-quartet ground state with  $A_2$  orbital symmetry ( ${}^4A_2$ ), arising from five electrons localized on the four carbon dangling bonds surrounding the vacancy. The lowest-energy optical excitation corresponds to promoting one electron from the  $a_1(u)$  orbital to  $a_1(v)$  in the spin-minority channel [see Fig. 1(b)], giving rise to an excited  ${}^4A_2'$  state. Both states retain  $C_{3v}$  symmetry in the unstrained crystal [40], which gets reduced to  $C_1$  under applied uniaxial strain along the  $a$ -axis.

The calculated ZPL energies for the  ${}^4A_2' \rightarrow {}^4A_2$  optical transition obtained using the  $r^2$ SCAN functional are

TABLE I. Calculated ZPL shifts (in meV) for  $V_{\text{Si}}^-(h)$  and  $V_{\text{Si}}^-(k)$  under uniaxial strain along the  $a$ -axis of 4H-SiC and compared to experimental data.

Strain	$V_{\text{Si}}^-(h)$	$V_{\text{Si}}^-(k)$	Expt. [25]
-2%	26.3	35.7	26 ( $V_{\text{Si}}^-(h)$ , 6H-SiC)
+2%	-30.8	-43.3	

1.392 eV for  $V_{\text{Si}}^-(h)$  and 1.306 eV for  $V_{\text{Si}}^-(k)$ , which are in good agreement with the experimental V1 (1.439 eV) and V2 (1.353 eV) values, respectively. Application of uniaxial strain along the crystallographic  $a$ -axis of 4H-SiC results in substantial shifting of the emission energies for both configurations. The calculated ZPL energy shifts for  $V_{\text{Si}}^-(h)$  and  $V_{\text{Si}}^-(k)$  are contained in Table I. Notably, the calculated shift in  $V_{\text{Si}}^-(h)$  emission energy of 26.3 meV is in excellent agreement with experimental data, where a 26 meV ZPL shift was observed for the  $V_{\text{Si}}^-(h)$  defect in 6H-SiC microparticles and attributed to  $-2\%$  compressive strain along the particle's  $a$ -axis [25], in support of the chosen methodology.

## B. Vibrational properties

Phonon sidebands in the emission spectrum arise from vibrational excitations following the optical transition. They are quantitatively described by the spectral function of electron-phonon coupling  $S(\hbar\omega)$ , which characterizes the average number of phonons emitted within a given energy interval. Figures 2(a)–2(f) present the spectral functions of electron-phonon coupling, together with corresponding shapes of collective vibrations that govern the emission of the  $V_{\text{Si}}^-$  defect in 4H-SiC under zero strain and uniaxial strain along the  $a$ -axis. Panels (a)–(c) correspond to the hexagonal configuration  $V_{\text{Si}}^-(h)$ , whereas panels (d)–(f) display the results for the quasicubic configuration  $V_{\text{Si}}^-(k)$ . The three columns represent strain-free (0%, black curves), tensile (+2%, blue curves), and compressive ( $-2\%$ , orange curves) conditions, respectively. Across both configurations, two vibrational features dictate the electron-phonon coupling: delocalized bulk-like modes in the range of 30–50 meV, and higher-energy quasi-localized modes within the 67–83 meV range. These quasi-local modes are associated with the motion of a neighboring carbon atom vibrating along the principal  $c$ -axis towards the silicon vacancy site and vibrations of three nearest neighbor silicon atoms. For the  $V_{\text{Si}}^-(h)$  configuration, the neighboring carbon atom is at the  $h$  lattice site and its three nearest silicon neighbors are located at  $k$  symmetry sites. In contrast, for  $V_{\text{Si}}^-(k)$ , the vibrations are centered on the neighboring carbon atom at the  $k$  lattice site and its adjacent silicon atoms at  $h$  sites.

In the absence of strain, the electron-phonon coupling exhibits pronounced differences between the two defect configurations. For  $V_{\text{Si}}^-(h)$ , the spectral function is dominated by a low-energy peak at approximately 38.4 meV, accompanied by a sharp split feature at 74.6 and 76.7 meV. In contrast, the  $V_{\text{Si}}^-(k)$  displays a distinctly different response, characterized by a double-peak structure at 38.2 and 43.3 meV, while exhibiting a single dominant sharp feature at approximately 75.8 meV. These distinctions in the electron-phonon coupling are also reflected in the experimental emission spectra discussed further below.

Under uniaxial strain applied along the  $a$ -axis, the vibrational structure evolves as follows. The bulk-like vibrational modes show marginal variations in their electron-phonon coupling peak positions, indicating weak sensitivity to strain. This is consistent with the negligible changes in the calculated bulk phonon density of states (DOS) in the acoustic regime (see Fig. S3 of the Supplemental Material). The quasi-local modes shift to lower energies under  $+2\%$  tensile strain, whereas under  $-2\%$  compressive strain they shift toward higher energies. A notable exception occurs for  $V_{\text{Si}}^-(h)$  under  $+2\%$  strain [see Fig. 2(b)], where the vibration of the neighboring carbon atom no longer occurs along the  $c$ -axis but instead involves the carbon atom at the  $k$  site and three neighboring silicon atoms (two at  $h$  sites and one at a  $k$  site). This strain-induced modification renders the hexagonal configuration more similar to the quasicubic configuration, leading to a splitting of the bulk-like electron-phonon coupling feature and a single quasi-local vibrational peak.

The calculated total Huang-Rhys (HR) factor [41], defined as  $S_{\text{tot}} = \sum_k S_k$ , quantifies the overall strength of electron-phonon coupling through the cumulative contribution of all vibrational modes  $k$ . For the hexagonal configuration, the  $S_{\text{tot}}$  were determined to be 3.04, 2.98, and 3.54 under 0%,  $+2\%$ , and  $-2\%$  uniaxial strain along the  $a$ -axis, respectively. In the quasicubic configuration, the  $S_{\text{tot}}$  were 2.88, 3.13, and 3.32 for the respective strain conditions (see also legends in Fig. 2). The calculated mass-weighted displacement  $\Delta Q$  ( $\text{amu}^{0.5} \text{\AA}$ ) between the ground- and excited-state equilibrium geometries for  $V_{\text{Si}}^-(h)$  was 0.698 at zero strain, decreasing to 0.642 under  $+2\%$  strain, and increasing to 0.718 under  $-2\%$  strain. In contrast,  $V_{\text{Si}}^-(k)$  exhibits a weaker strain dependence, with  $\Delta Q$  values of 0.684, 0.680, and 0.705 for 0%,  $+2\%$ , and  $-2\%$  strain, respectively. Tensile strain reduces the coupling to defect modes by increasing ion-ion separations around the vacancy site, while simultaneously enhancing coupling to low-energy bulk-like vibrational modes. For  $V_{\text{Si}}^-(k)$ , the weaker strain dependence of  $\Delta Q$  is insufficient to compensate for this bulk contribution, resulting in a net increase of  $S_{\text{tot}}$  under  $+2\%$  strain. In contrast,  $V_{\text{Si}}^-(h)$  exhibits stronger change of  $\Delta Q$ , leading to an overall reduction of  $S_{\text{tot}}$  under  $+2\%$  strain.

## C. Optical lineshapes under strain

Figure 3 shows calculated emission lineshapes for  $V_{\text{Si}}^-(h)$  and  $V_{\text{Si}}^-(k)$  defects under zero strain conditions and uniaxial strain applied along the  $a$ -axis. The curves correspond to strain-free (0%, black curves), tensile ( $+2\%$ , blue curves), and compressive ( $-2\%$ , orange curves) conditions. The PSB observed in all spectra originates from bulk-like, quasi-local and localized vibrational modes and their respective replicas, with the PSB governed by the bulk-like and quasi-local contributions. All

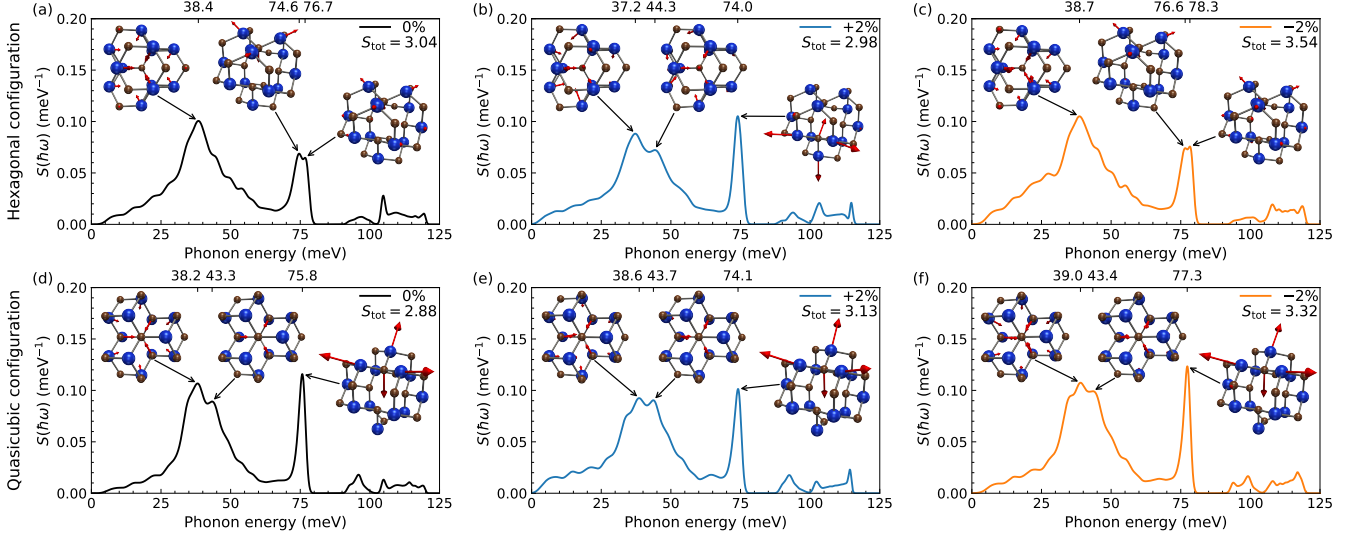


FIG. 2. Spectral functions of electron-phonon coupling  $S(\hbar\omega)$  (in  $\text{meV}^{-1}$ ) for the emission of the  $V_{\text{Si}}^-$  defect in 4H-SiC under uniaxial strain applied along the  $a$ -axis. Panels (a)–(c) correspond to the hexagonal  $V_{\text{Si}}^-(h)$  configuration, while (d)–(f) show results for the quasicubic  $V_{\text{Si}}^-(k)$  configuration. Each column shows results for strain magnitudes of 0%, +2%, and –2%, respectively. Insets illustrate the effective shapes of collective vibrations corresponding to delocalized bulk-like and quasi-localized modes. Amplitudes are scaled for visual clarity.

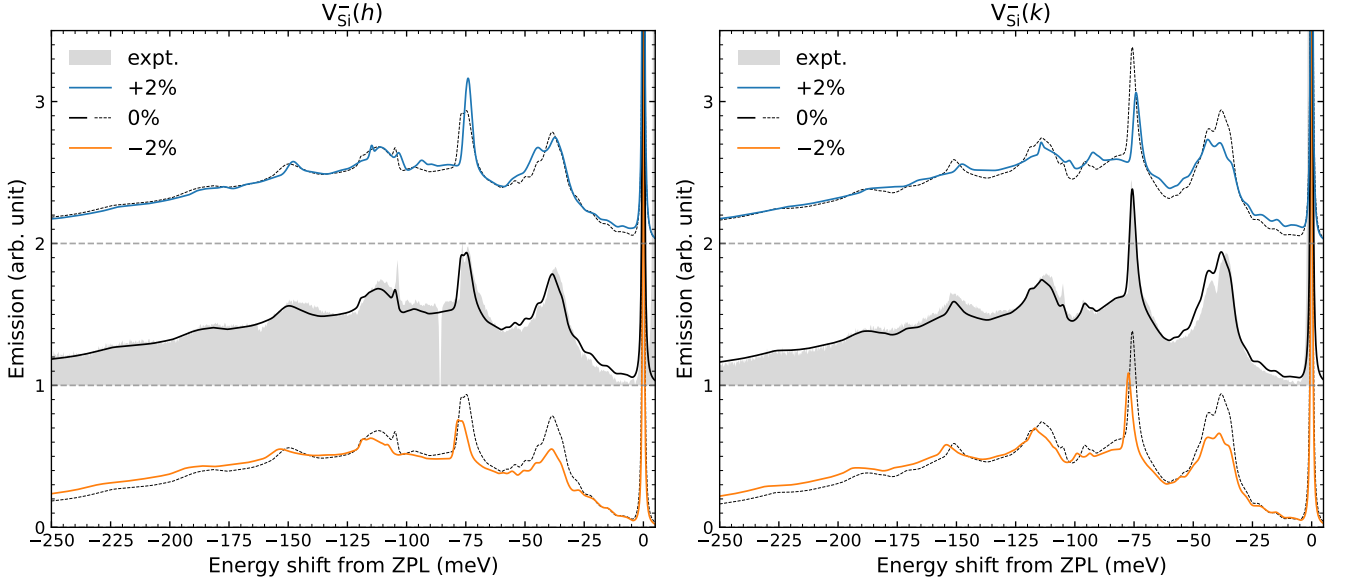


FIG. 3. Calculated emission lineshapes for supercells with  $V_{\text{Si}}^-(h)$  and  $V_{\text{Si}}^-(k)$  defects with zero (middle panels, black curves), +2% (top panels, blue curves) and –2% (bottom panels, orange curves) uniaxial strain applied along  $a$ -axis. The shaded gray areas in the middle panels represent experimental data measured on  $V_{\text{Si}}^-$  ensembles for the strain-free case. Calculated strain-free lineshapes are also shown as black dotted lines in the top and bottom panels, allowing comparison with the calculated strained lineshapes. Emission lineshapes were computed with the  $r^2\text{SCAN}$  functional using HR theory and extrapolated to the dilute limit, approximated by a  $25 \times 25 \times 8$  supercell with 40 000 atomic sites.

PSB peak positions will be given in units of meV below the ZPL. Strain-induced shifts of characteristic emission peaks can be identified in the PSB, reflecting the varying strain sensitivity of different phonon modes.

At zero strain, the calculated lineshapes (black lines)

closely follow the experimental data (gray shaded areas in Fig. 3). In particular, they reproduce the characteristic double-peak of the quasi-local vibrational modes for  $V_{\text{Si}}^-(h)$ , observed at (74.0, 76.4) meV, as well as the double-peak of bulk-like vibrational modes for  $V_{\text{Si}}^-(k)$  at

(36.2, 42.0) meV. This demonstrates that ensemble measurements based on stimulated emission can be directly compared with theoretically computed lineshapes when the ZPLs of different defect configurations are well separated and do not overlap with prominent vibrational features of other configurations.

For  $V_{\text{Si}}^-(h)$ , the calculated unstrained emission spectrum features a prominent PSB peak at 38.5 meV arising from bulk-like vibrational modes, as well as a double-peak at (74.8, 76.6) meV associated with quasi-local vibrational modes. Under  $-2\%$  compressive strain, these features shift to higher energies, appearing at 38.8 meV and (76.8, 78.2) meV. Under  $+2\%$  tensile strain, the bulk-like peak splits into a double peak of (37.3, 44.5) meV, while the quasi-local mode double-peak collapses into a single peak at 74.0 meV, due to increased resonance with the bulk phonon modes. A faint feature corresponding to the phonon replica of the quasi-local mode is calculated to be at 149.6, 147.8, and 153.2 meV for 0%,  $+2\%$ , and  $-2\%$  strain, respectively.

In contrast,  $V_{\text{Si}}^-(k)$  exhibits a double-peak structure in the bulk-like vibrational region, with features calculated at (38.2, 43.3) meV, while the quasi-local vibrational mode appears as a single peak at 75.8 meV. Under  $+2\%$  tensile strain, these features shift to (38.8, 43.9) meV and 74.2 meV, whereas under  $-2\%$  compressive strain they move to higher energies of (39.1, 43.7) meV and 77.4 meV. The quasi-local phonon replica is calculated to be at 151.1, 147.6, and 154.2 meV for 0%,  $+2\%$ , and  $-2\%$  strain, respectively.

The first PSB peak associated with bulk-like vibrational modes shows minor energy shifts under strain consistent with changes in the bulk phonon DOS (see Fig. S3 of the Supplemental Material). Stronger shifts are predicted for the second PSB peak associated with quasi-local vibrational modes. In both  $V_{\text{Si}}^-$  configurations, the second PSB peak shifts closer to the ZPL under tensile ( $+2\%$ ) strain and away from it under compressive ( $-2\%$ ) strain. Finally, the PSB feature near 150 meV, arising from the phonon replica of quasi-local modes, undergoes the largest strain-induced shifts among all observed peaks.

The Debye–Waller factor (DWF) is defined as the ratio of the ZPL intensity to the total emission lineshape and is an important quantum emitter characteristic. The calculated DWF values for  $V_{\text{Si}}^-$  defects under different strain conditions are presented in Table II. For the hexagonal configuration, the calculated DWF values are 6.61%, 6.95%, and 4.18% at 0%,  $+2\%$ , and  $-2\%$  strain, respectively. Thus, strain can be utilized to enhance the DWF, as exemplified by the  $+2\%$  condition. In the quasicubic configuration, the DWF values are 7.77%, 6.09%, and 5.27% for the same strain values. These results are consistent with the HR factor trends, as stronger electron–phonon coupling leads to a reduction in the ZPL intensity and, consequently, a lower DWF.

TABLE II. Computed mass-weighted displacements ( $\Delta Q$ , in  $\text{amu}^{0.5} \text{\AA}$ ), total Huang–Rhys factors ( $S_{\text{tot}}$ ), and Debye–Waller factors (DWF, in %) for the emission of  $V_{\text{Si}}^-$  defects in 4H-SiC under  $\pm 2\%$  uniaxial strain along the  $a$ -axis.

Strain	$V_{\text{Si}}^-(h)$			$V_{\text{Si}}^-(k)$		
	$\Delta Q$	$S_{\text{tot}}$	DWF	$\Delta Q$	$S_{\text{tot}}$	DWF
0%	0.698	3.04	6.61	0.684	2.88	7.77
$+2\%$	0.642	2.98	6.95	0.680	3.13	6.09
$-2\%$	0.718	3.54	4.18	0.705	3.32	5.27

#### IV. CONCLUSIONS

We have presented a first-principles investigation of the vibrational structure and emission lineshapes of  $V_{\text{Si}}^-$  centers in 4H-SiC under uniaxial tensile and compressive strain applied along the  $a$ -axis. At zero strain, the calculated emission lineshapes are in excellent agreement with experimental spectra, reproducing the characteristic double-peak features associated with quasi-local modes for  $V_{\text{Si}}^-(h)$  and bulk-like modes for  $V_{\text{Si}}^-(k)$ , validating the theoretical framework. The calculated emission spectra show that bulk-like modes are weakly affected by strain, whereas quasi-local, quasi-local replica, and localized modes exhibit clear, directional energy shifts under tensile and compressive strain. The emission lineshapes were modeled at 0 K, where fine features of the PSB are resolved. At higher temperatures, thermal broadening is expected to obscure finer details related to localized modes or quasi-local mode replicas. Consequently, the second PSB peak emerges as a robust spectral feature for strain calibration in  $V_{\text{Si}}^-$  centers. Nonetheless, overall PSB energy shifts remain a clear indicator of whether the defect experiences tensile or compressive strain along the  $a$ -axis.

In addition to spectral shifts, we find that uniaxial strain can beneficially impact the electron–phonon coupling. For the hexagonal  $V_{\text{Si}}^-(h)$  configuration,  $+2\%$  tensile strain along the  $a$ -axis leads to a reduction of the overall coupling strength and an increased DWF, indicating that strain can be employed as an external means to enhance quantum emitter performance. Taken together, our results establish that strain-dependent phonon sidebands, combined with ZPL shifts, provide a multidimensional and magnetic-field-free readout mechanism for strain sensing using spin-conserving optical transitions.

#### ACKNOWLEDGMENTS

The work of MEB was supported by an ETH Zürich Postdoctoral Fellowship. Financial support was kindly provided by the Research Council of Norway and the University of Oslo through the frontier research projects QuTe (no. 325573, FriPro ToppForsk-program) and TASQ (no. 354419, FriPro). RU acknowledges funding by the Max-Planck Society. The computations were

performed on resources provided by UNINETT Sigma2 — the National Infrastructure for High Performance Computing and Data Storage in Norway, supercomputer GALAX of the Center for Physical Sciences and Technology, Lithuania, and the High Performance Computing Center “HPC Saulėtekis” in the Faculty of Physics, Vilnius University.

## AUTHOR CONTRIBUTIONS

MEB designed the research with support from LR, UG and LV. VŽ, RS and MEB performed the calculations. VŽ, RS, and LR wrote the codes for lineshape calculations and embedding methodology. VŽ, RS, LR and MEB analyzed the data. RU supervised the experimental part. ATY and MTL performed the experiments. All authors have contributed to the discussion and interpretation of the results. VŽ wrote the manuscript with support and editing from all authors.

- 
- [1] C. L. Degen, F. Reinhard, and P. Cappellaro, Quantum sensing, *Reviews of Modern Physics* **89**, 035002 (2017).
- [2] D. D. Awschalom, R. Hanson, J. Wrachtrup, and B. B. Zhou, Quantum technologies with optically interfaced solid-state spins, *Nature Photonics* **12**, 516 (2018).
- [3] D. M. Toyli, C. F. de Las Casas, D. J. Christle, V. V. Dobrovitski, and D. D. Awschalom, Fluorescence thermometry enhanced by the quantum coherence of single spins in diamond, *Proceedings of the National Academy of Sciences* **110**, 8417 (2013).
- [4] G. Kucsko, P. C. Maurer, N. Y. Yao, M. Kubo, H. J. Noh, P. K. Lo, H. Park, and M. D. Lukin, Nanometrescale thermometry in a living cell, *Nature* **500**, 54 (2013).
- [5] M. W. Doherty, V. V. Struzhkin, D. A. Simpson, L. P. McGuinness, Y. Meng, A. Stacey, T. J. Karle, R. J. Hemley, N. B. Manson, L. C. Hollenberg, *et al.*, Electronic properties and metrology applications of the diamond NV<sup>-</sup> center under pressure, *Physical Review Letters* **112**, 047601 (2014).
- [6] B. Vindolet, M.-P. Adam, L. Toraille, M. Chipaux, A. Hilberer, G. Dupuy, L. Razinkovas, A. Alkauskas, G. Thiering, A. Gali, *et al.*, Optical properties of SiV and GeV color centers in nanodiamonds under hydrostatic pressures up to 180 GPa, *Physical Review B* **106**, 214109 (2022).
- [7] A. Hilberer, L. Toraille, C. Dailedouze, M.-P. Adam, L. Hanlon, G. Weck, M. Schmidt, P. Loubeyre, and J.-F. Roch, Enabling quantum sensing under extreme pressure: Nitrogen-vacancy magnetometry up to 130 GPa, *Physical Review B* **107**, L220102 (2023).
- [8] F. Dolde, H. Fedder, M. W. Doherty, T. Nöbauer, F. Rempp, G. Balasubramanian, T. Wolf, F. Reinhard, L. C. Hollenberg, F. Jelezko, *et al.*, Electric-field sensing using single diamond spins, *Nature Physics* **7**, 459 (2011).
- [9] L. Alaerts, Y. Xiong, S. Griffin, and G. Hautier, First-principles study of the Stark shift effect on the zero-phonon line of the NV center in diamond, *Physical Review Materials* **8**, 106201 (2024).
- [10] L. Rondin, J.-P. Tetienne, T. Hingant, J.-F. Roch, P. Maletinsky, and V. Jacques, Magnetometry with nitrogen-vacancy defects in diamond, *Reports on Progress in Physics* **77**, 056503 (2014).
- [11] L. Razinkovas, M. W. Doherty, N. B. Manson, C. G. Van de Walle, and A. Alkauskas, Vibrational and vibronic structure of isolated point defects: The nitrogen-vacancy center in diamond, *Physical Review B* **104**, 045303 (2021).
- [12] Y. Jin, M. Govoni, G. Wolfowicz, S. E. Sullivan, F. J. Heremans, D. D. Awschalom, and G. Galli, Photoluminescence spectra of point defects in semiconductors: Validation of first-principles calculations, *Physical Review Materials* **5**, 084603 (2021).
- [13] Y. Jin, M. Govoni, and G. Galli, Vibrationally resolved optical excitations of the nitrogen-vacancy center in diamond, *npj Computational Materials* **8**, 238 (2022).
- [14] R. Silkinis, M. Maciaszek, V. Žalandauskas, M. E. Bathen, L. Vines, A. Alkauskas, and L. Razinkovas, Optical lineshapes of the C center in silicon from ab initio calculations: Interplay of localized modes and bulk phonons, *Physical Review B* **111**, 125136 (2025).
- [15] C. Linderälv, N. Österbacka, J. Wiktor, and P. Erhart, Optical line shapes of color centers in solids from classical autocorrelation functions, *npj Computational Materials* **11**, 101 (2025).
- [16] M. E. Turiansky, J. L. Lyons, and N. Bernstein, Machine learning phonon spectra for fast and accurate optical lineshapes of defects, *arXiv preprint arXiv:2508.09113* (2025).
- [17] M. W. Doherty, N. B. Manson, P. Delaney, F. Jelezko, J. Wrachtrup, and L. C. Hollenberg, The nitrogen-vacancy colour centre in diamond, *Physics Reports* **528**, 1 (2013).
- [18] M. Widmann, S.-Y. Lee, T. Rendler, N. T. Son, H. Fedder, S. Paik, L.-P. Yang, N. Zhao, S. Yang, I. Booker, *et al.*, Coherent control of single spins in silicon carbide at room temperature, *Nature Materials* **14**, 164 (2015).
- [19] D. J. Christle, A. L. Falk, P. Andrich, P. V. Klimov, J. U. Hassan, N. T. Son, E. Jánzén, T. Ohshima, and D. D. Awschalom, Isolated electron spins in silicon carbide with millisecond coherence times, *Nature Materials* **14**, 160 (2015).
- [20] C. F. de las Casas, D. J. Christle, J. Ul Hassan, T. Ohshima, N. T. Son, and D. D. Awschalom, Stark tuning and electrical charge state control of single divacancies in silicon carbide, *Applied Physics Letters* **111**, 262403 (2017).
- [21] M. E. Bathen, A. Galeckas, J. Müting, H. M. Ayedh, U. Grossner, J. Coutinho, Y. K. Frodason, and L. Vines, Electrical charge state identification and control for the silicon vacancy in 4H-SiC, *npj Quantum Information* **5**, 111 (2019).
- [22] P. Udvarhelyi, G. Thiering, N. Morioka, C. Babin, F. Kaiser, D. Lukin, T. Ohshima, J. Ul-Hassan, N. T. Son, J. Vučković, *et al.*, Vibronic states and their ef-

- fect on the temperature and strain dependence of silicon-vacancy qubits in 4H-SiC, *Physical Review Applied* **13**, 054017 (2020).
- [23] M. Rühl, L. Bergmann, M. Krieger, and H. B. Weber, Stark tuning of the silicon vacancy in silicon carbide, *Nano Letters* **20**, 658 (2020).
- [24] C. P. Anderson, A. Bourassa, K. C. Miao, G. Wolfowicz, P. J. Mintun, A. L. Crook, H. Abe, J. Ul Hassan, N. T. Son, T. Ohshima, *et al.*, Electrical and optical control of single spins integrated in scalable semiconductor devices, *Science* **366**, 1225 (2019).
- [25] G. C. Vásquez, M. E. Bathen, A. Galeckas, C. Bazioti, K. Johansen, D. Maestre, A. Cremades, Ø. Prytz, A. Moe, A. Y. Kuznetsov, *et al.*, Strain modulation of Si vacancy emission from SiC micro- and nanoparticles, *Nano Letters* **20**, 8689 (2020).
- [26] S. Castelletto, C. T.-K. Lew, W.-X. Lin, and J.-S. Xu, Quantum systems in silicon carbide for sensing applications, *Reports on Progress in Physics* **87**, 014501 (2023).
- [27] G. Kresse and J. Hafner, Ab initio molecular dynamics for liquid metals, *Physical Review B* **47**, 558 (1993).
- [28] G. Kresse and J. Hafner, Ab initio molecular-dynamics simulation of the liquid-metal–amorphous-semiconductor transition in germanium, *Physical Review B* **49**, 14251 (1994).
- [29] G. Kresse and J. Furthmüller, Efficiency of ab-initio total energy calculations for metals and semiconductors using a plane-wave basis set, *Computational Materials Science* **6**, 15 (1996).
- [30] P. E. Blöchl, Projector augmented-wave method, *Physical Review B* **50**, 17953 (1994).
- [31] G. Kresse and J. Furthmüller, Efficient iterative schemes for ab initio total-energy calculations using a plane-wave basis set, *Physical Review B* **54**, 11169 (1996).
- [32] J. W. Furness, A. D. Kaplan, J. Ning, J. P. Perdew, and J. Sun, Accurate and numerically efficient  $r^2$ SCAN meta-generalized gradient approximation, *The Journal of Physical Chemistry Letters* **11**, 8208 (2020).
- [33] G. Abbas, O. Bulancea-Lindvall, J. Davidsson, R. Armiento, and I. A. Abrikosov, Theoretical characterization of NV-like defects in 4H-SiC using ADAQ with SCAN and  $r^2$ SCAN meta-GGA functionals, *Applied Physics Letters* **126**, 154001 (2025).
- [34] V. Žalandauskas, R. Silkinis, L. Vines, L. Razinkovas, and M. E. Bathen, Theory of the divacancy in 4H-SiC: impact of Jahn-Teller effect on optical properties, *npj Computational Materials* **11**, 155 (2025).
- [35] A. Togo and I. Tanaka, First principles phonon calculations in materials science, *Scripta Materialia* **108**, 1 (2015).
- [36] A. Alkauskas, B. B. Buckley, D. D. Awschalom, and C. G. Van de Walle, First-principles theory of the luminescence lineshape for the triplet transition in diamond NV centres, *New Journal of Physics* **16**, 073026 (2014).
- [37] A. T. Younesi and R. Ulbricht, Broadband transient absorption spectroscopy using an incoherent white-light source as probe, *Optics Express* **30**, 38896 (2022).
- [38] M. T. Luu, A. T. Younesi, and R. Ulbricht, Nitrogen-vacancy centers in diamond: discovery of additional electronic states, *Materials for Quantum Technology* **4**, 035201 (2024).
- [39] A. T. Younesi, M. T. Luu, C. Linderälv, V. Žalandauskas, M. E. Bathen, N. T. Son, T. Ohshima, G. Thiering, L. Razinkovas, and R. Ulbricht, Unraveling the electronic structure of silicon vacancy centers in 4H-SiC, arXiv preprint arXiv:2602.14818 (2026).
- [40] Ö. Soykal, P. Dev, and S. E. Economou, Silicon vacancy center in 4H-SiC: Electronic structure and spin-photon interfaces, *Physical Review B* **93**, 081207 (2016).
- [41] K. Huang and A. Rhys, Theory of light absorption and non-radiative transitions in F-centres, *Proceedings of the Royal Society of London. Series A. Mathematical and Physical Sciences* **204**, 406 (1950).
- [42] A. Gali, E. Janzén, P. Deák, G. Kresse, and E. Kaxiras, Theory of spin-conserving excitation of the NV center in diamond, *Physical Review Letters* **103**, 186404 (2009).
- [43] Y. Zhu, B. Kovos, M. Onizhuk, D. Awschalom, and G. Galli, Theoretical and experimental study of the nitrogen-vacancy center in 4h-sic, *Physical Review Materials* **5**, 074602 (2021).
- [44] W. Choyke and G. Pensl, Physical properties of SiC, *MRS Bulletin* **22**, 25 (1997).
- [45] A. Csóré, N. Son, and A. Gali, Towards identification of silicon vacancy-related electron paramagnetic resonance centers in 4H-SiC, *Physical Review B* **104**, 035207 (2021).
- [46] J. Davidsson, R. Babar, D. Shafizadeh, I. G. Ivanov, V. Ivády, R. Armiento, and I. A. Abrikosov, Exhaustive characterization of modified Si vacancies in 4H-SiC, *Nanophotonics* **11**, 4565 (2022).
- [47] V. Ivády, J. Davidsson, N. T. Son, T. Ohshima, I. A. Abrikosov, and A. Gali, Identification of Si-vacancy related room-temperature qubits in 4H silicon carbide, *Physical Review B* **96**, 161114 (2017).
- [48] A. Hashemi, C. Linderälv, A. V. Krasheninnikov, T. AlaNissila, P. Erhart, and H.-P. Komsa, Photoluminescence line shapes for color centers in silicon carbide from density functional theory calculations, *Physical Review B* **103**, 125203 (2021).
- [49] Z. Shang, A. Hashemi, Y. Berencén, H.-P. Komsa, P. Erhart, S. Zhou, M. Helm, A. V. Krasheninnikov, and G. V. Astakhov, Local vibrational modes of Si vacancy spin qubits in SiC, *Physical Review B* **101**, 144109 (2020).
- [50] J. J. Markham, Interaction of normal modes with electron traps, *Reviews of Modern Physics* **31**, 956 (1959).
- [51] R. Kubo and Y. Toyozawa, Application of the Method of Generating Function to Radiative and Non-Radiative Transitions of a Trapped Electron in a Crystal, *Progress of Theoretical Physics* **13**, 160 (1955).
- [52] M. Lax, The Franck-Condon Principle and Its Application to Crystals, *The Journal of Chemical Physics* **20**, 1752 (1952).
- [53] R. J. Bell, P. Dean, and D. C. Hibbins-Butler, Localization of normal modes in vitreous silica, germania and beryllium fluoride, *Journal of Physics C: Solid State Physics* **3**, 2111 (1970).
- [54] M. T. Luu, C. Linderälv, Z. Benedek, Á. Ganyecz, G. Barcza, V. Ivády, and R. Ulbricht, Identifying high-energy electronic states of NV<sup>-</sup> centers in diamond, *Applied Physics Letters* **126**, 234001 (2025).

## SUPPLEMENTAL MATERIAL

## S1 ELECTRONIC STRUCTURE AND ZERO-PHONON LINE ENERGIES

The electronic structure of both silicon vacancy configurations in 4H-SiC can be understood in terms of four carbon dangling bonds surrounding the vacant silicon site [40]. These combine to form four molecular orbitals: two  $a_1$  states (a lower-lying  $a_1(u)$ , a higher-lying  $a_1(v)$ ) state, and a pair of degenerate orbitals with  $e$  symmetry within the band gap (see Fig. 1(b) from main text). In the negatively charged state that exhibits bright emission, five electrons occupy these orbitals. The ground state of the defect is a spin-quartet with  $A_2$  orbital symmetry ( ${}^4A_2$ ), described by a single-determinant wave function  $|a_1(u) \bar{a}_1(u) a_1(v) e_x e_y|$  for the spin projection  $m_s = 3/2$ . The first excited state  ${}^4A_2'$  can be represented by a single-determinant wave function  $|a_1(u) a_1(v) \bar{a}_1(v) e_x e_y|$  for the same spin projection. Both states exhibit  $C_{3v}$  point-group symmetry characterized by a threefold rotation axis  $C_3$  oriented along the crystallographic  $c$ -axis, and three vertical mirror planes  $\sigma_v$ . When uniaxial strain is applied along the  $a$ -axis, the threefold rotational symmetry and all mirror symmetries are lifted. As a result, the symmetry is reduced to the trivial point group  $C_1$ , and all orbitals transform according to the totally symmetric representation  $a$ .

The ZPL energies were computed using the  $\Delta$ -self-consistent-field ( $\Delta$ SCF) approach [42], whose reliability has been demonstrated for a variety of point defects in 4H-SiC [12, 33, 34, 43]. The excited state was constructed by constraining the Kohn–Sham single-particle level occupancies and promoting one electron from the highest occupied level in the spin-minority channel to the next higher-energy level within the same spin channel. In the zero strain case, this corresponds to a promotion of an electron from the  $a_1(u)$  defect level to the nearest higher-lying  $a_1(v)$  defect level in the spin-minority channel. Under uniaxial strain, the excitation is modeled by promoting an electron from the highest occupied  $a$ -symmetry defect orbital to the nearest higher-lying unoccupied  $a$ -symmetry defect level within the spin-minority channel.

Table S1 presents a comparison between the calculated and experimental ZPL energies for the  $V_{\text{Si}}^-(h)$  and  $V_{\text{Si}}^-(k)$  defects in 4H-SiC. Previously reported theoretical ZPL values are also included, along with brief computational details provided below the table. The meta-GGA  $r^2$ SCAN functional underestimates the ZPL energies by 0.069 eV and 0.068 eV for the  $V_{\text{Si}}^-(h)$  and  $V_{\text{Si}}^-(k)$  defects, respectively. For comparison, previous theoretical studies employing the PBE functional report larger underestimations, ranging from 0.119 to 0.194 eV for  $V_{\text{Si}}^-(h)$  and from 0.093 to 0.155 eV for  $V_{\text{Si}}^-(k)$ . Despite the fact that  $r^2$ SCAN underestimates the bulk 4H-SiC band gap (2.223 eV for PBE, 2.611 eV for  $r^2$ SCAN, 3.172 eV for HSE06, and 3.265 eV from experiment [44]), it nevertheless yields ZPL energies that come close to the experimental values, while requiring  $\approx 40$  times less computational effort than the hybrid HSE06 functional for the same supercell size and Brillouin zone sampling.

TABLE S1. Comparison of calculated and experimental zero-phonon line (ZPL) energies (in units of eV) for spin-conserving transitions for the negatively charged silicon vacancy centers in 4H-SiC. Previous theoretically predicted ZPL energies are also shown.

	This work	Previous theoretical work			Expt.
	$r^2$ SCAN	PBE	HSE06		
$V_{\text{Si}}^-(h)$	1.392	1.273 <sup>a</sup> , 1.245 <sup>b</sup>	1.450 <sup>a</sup> , 1.376 <sup>b</sup> , 1.541 <sup>c</sup> , 1.450 <sup>d</sup> , 1.57 <sup>e</sup>		1.439
$V_{\text{Si}}^-(k)$	1.306	1.198 <sup>a</sup> , 1.175 <sup>b</sup>	1.385 <sup>a</sup> , 1.283 <sup>b</sup> , 1.443 <sup>c</sup> , 1.385 <sup>d</sup> , 1.24 <sup>e</sup> , 1.35 <sup>f</sup>		1.353

<sup>a</sup>Reference [45]: Calculations were carried out using VASP code with PAW pseudopotentials (PPs). The plane-wave energy cutoff was set to 420 eV. The Brillouin zone was sampled with the  $\Gamma$  point. 1536 atom supercell was used. The ZPL values with the HSE06 functional were obtained by correcting the corresponding PBE result with the difference of the isolated  $V_{\text{Si}}^-$ -related PBE and HSE06 ZPL values as an estimate.

<sup>b</sup>Reference [46]: Calculations were carried out using VASP code with PAW PPs. The plane-wave energy cutoff was set to 600 eV for PBE and 420 eV for HSE06 functional. The Brillouin zone was sampled with the  $\Gamma$  point. 2304 atom supercell was used for PBE functional while 576 atom supercell was used for HSE06.

<sup>c</sup>Reference [47]: Calculations were carried out using VASP code with PAW PPs. The plane-wave energy cutoff was set to 390 eV. The Brillouin zone was sampled with the  $\Gamma$  point. 1536 atom supercell was used.

<sup>d</sup>Reference [22]: Calculations were carried out using the VASP code with PAW PPs. The plane-wave energy cutoff was set to 420 eV. The Brillouin zone was sampled with the  $\Gamma$  point. 768 atom supercell was used.

<sup>e</sup>Reference [48]: Calculations were carried out using VASP code with PAW PPs. The plane-wave energy cutoff was set to 400 eV. The Brillouin zone was sampled with the  $\Gamma$  point. 400 atom supercell was used.

<sup>f</sup>Reference [49]: Calculations were carried out using VASP code with PAW PPs. The plane-wave energy cutoff was set to 450 eV. The Brillouin zone was sampled using a  $2 \times 2 \times 2$   $k$ -point mesh. 400 atom supercell was used.

## S2 THEORETICAL DESCRIPTION OF ELECTRON-PHONON INTERACTION

In the the Franck-Condon approximation, the normalized lineshape for emission and absorption at absolute zero temperature ( $T = 0$  K) can be expressed as follows [11]:

$$L(\hbar\omega) = C\omega^\kappa A(\hbar\omega), \quad (\text{S1})$$

where  $C$  denotes a normalization constant,  $A(\hbar\omega)$  denotes the phonon spectral function, and the exponent  $\kappa$  is equal to 3 for emission and 1 for absorption. The spectral function is defined by the equation

$$A(\hbar\omega) = \sum_m |\langle \chi_{i;0} | \chi_{f;m} \rangle|^2 \delta(E_{\text{ZPL}} \mp (\varepsilon_{f_m} - \varepsilon_{f_0}) - \hbar\omega), \quad (\text{S2})$$

where  $E_{\text{ZPL}}$  is the energy of the zero-phonon line (ZPL), while  $\chi_{i;0}$  and  $\chi_{f;m}$  represent the vibrational wave functions corresponding to the initial and final electronic states. Here,  $\varepsilon_{f_m}$  refers to the energy of the  $m$ -th vibrational state within the final electronic manifold relative to the potential energy minimum. The signs in front of the  $\delta$ -function argument differentiate between emission (minus sign) and absorption (plus sign). The optical spectral function  $A(\hbar\omega)$  quantifies the transition amplitudes among vibrational states and plays a crucial role in determining the lineshape.

Due to the inherent differences in vibrational structures between the ground and excited states, the overlap integrals  $\langle \chi_{i;0} | \chi_{f;m} \rangle$  found in Eq. (S2) are multidimensional. Given the complexity with numerous vibrational modes in defect systems, directly calculating these integrals proves computationally challenging. To circumvent these difficulties and streamline the evaluation of overlap integrals, we utilize the equal-mode approximation from Ref. [11, 50], which assumes that both the shapes and frequencies of vibrational modes in the initial and final states are equivalent. To mitigate the drawbacks of this approximation, we consistently adopt the vibrational modes of the final state in our lineshape calculations, following guidelines from Ref. [11].

The spectral function  $A(\hbar\omega)$  can be effectively derived by calculating it in the time domain via the generating function approach established by Kubo and Lax [51, 52]. In this framework,  $A(\hbar\omega)$  is extracted from the generating function  $G(t)$  according to the following expression:

$$A(\hbar\omega) = \frac{1}{2\pi} \int_{-\infty}^{\infty} G(t) e^{-\gamma|t|} e^{-i(E_{\text{ZPL}}/\hbar - \omega)t} dt, \quad (\text{S3})$$

where the term  $e^{-\gamma|t|}$  serves as a phenomenological adjustment to incorporate the homogeneous Lorentzian broadening of the ZPL that is not captured by this theoretical framework, in addition to addressing the effects of inhomogeneous broadening. The parameter  $\gamma$  is fine-tuned to align with the experimentally observed linewidth of the ZPL. In all lineshape calculations the  $\gamma$  value was set to be 0.30 meV.

Under the equal mode approximation, the expression for the generating function  $G(t)$  can be represented as

$$G(t) = \exp \left[ -S_{\text{tot}} + \sum_k S_k e^{\pm i\omega_k t} \right], \quad (\text{S4})$$

where the plus sign is applicable for emission and the minus sign for absorption, with  $S_k$  denoting the partial Huang-Rhys (HR) factor, and the summation encompasses all vibrational modes within the system. The total coupling strength is denoted by  $S_{\text{tot}} = \sum_k S_k$ . The factor  $S_k$  quantifies the average number of excited phonons present during an optical transition [41], and is formulated as

$$S_k = \frac{\omega_k \Delta Q_k^2}{2\hbar}, \quad (\text{S5})$$

where  $\Delta Q_k$  is the ionic displacement along the  $k$ -th normal mode, prompted by an optical transition. More specifically,  $\Delta Q_k$  represents the projection of mass-weighted displacement between the ground and excited states onto the normalized phonon mode  $\eta_k$ :

$$\Delta Q_k = \sum_{m\alpha} \sqrt{M_m} \Delta R_{m\alpha} \eta_{k;m\alpha}. \quad (\text{S6})$$

In this equation,  $\Delta R_{m\alpha}$  indicates the displacement of atom  $m$  along the  $\alpha$  coordinate, while  $M_m$  is its corresponding mass.

To adequately describe the generating function in Eq. (S4) in larger systems, where one would expect a continuum of vibrational frequencies, we introduce the spectral density of electron–phonon coupling, also referred to as the spectral function of electron–phonon coupling:

$$S(\hbar\omega) \equiv \sum_k S_k \delta(\hbar\omega_k - \hbar\omega), \quad (\text{S7})$$

which enables us to rewrite the generating function in the following form:

$$G(t) = \exp \left[ -S_{\text{tot}} + \int S(\hbar\omega) e^{\pm i\omega t} d\omega \right]. \quad (\text{S8})$$

We used a Gaussian smoothing function to facilitate the approximation of the  $\delta$ -functions in Eq. (S7). This results in a smooth representation of the electron–phonon spectral function, where the  $\delta$ -functions are approximated using Gaussian functions with frequency-dependent widths  $\sigma$  that gradually decrease from 1.5 meV at zero frequency to 0.5 meV at the maximum phonon frequency for emission.

Phonon modes of 4H-SiC supercells containing the  $V_{\text{Si}}^-$  defects were calculated using the finite-displacement approach, with atomic configurations generated by the PHONOPY package [35]. A displacement amplitude of 0.01 Å from the equilibrium geometry was employed. The relatively small size of the computationally tractable supercells employed in this study results in the absence of low-frequency acoustic modes and a poor description of vibrational resonances. Experimentally measured ensemble defect concentrations typically range from  $1 \times 10^{12} \text{ cm}^{-3}$  to  $1 \times 10^{16} \text{ cm}^{-3}$ . The phonon modes were extrapolated to the dilute-defect limit using the force-constant embedding methodology described in Sec. S3.

An added challenge in supercell calculations occurs when determining the relaxation profile after an optical transition. The limited size of the supercell in direct calculations restricts the long-wavelength components of  $\Delta R_{m\alpha}$  in Eq. (S6). To accurately represent the relaxation profile in the dilute limit, we compute  $\Delta Q_k$  for each vibrational mode of a larger supercell (obtained through the embedding procedure) by employing forces and the harmonic relation to displacements. The relaxation component  $\Delta Q_k$  is calculated as follows:

$$\Delta Q_k = \frac{1}{\omega_k^2} \sum_{m\alpha} \frac{F_{m\alpha}}{\sqrt{M_m}} \eta_{k;m\alpha}, \quad (\text{S9})$$

where  $F_{m\alpha}$  denotes the force acting on atom  $m$  in the direction  $\alpha$  when the system is in the final electronic state, yet retains the equilibrium geometry of the initial state calculated in the directly accessible supercell. Here  $\eta_{k;m\alpha}$  is the vibrational mode shape as derived from the embedded supercell. By using forces that have already converged within the computationally tractable supercell, this strategy, in conjunction with the embedding methodology, effectively captures the electron–phonon coupling for low-frequency modes and offers an accurate description of the optical lineshapes.

In our calculations, the vibrational frequencies show very good agreement with experiment. However, with the  $r^2$ SCAN functional we observed an underestimation of atomic relaxations. We assume that the shape of the calculated spectral densities  $S(\hbar\omega)$  is close to the "truth", taking into account the positions of the peaks and the overall prediction of the vibrational structure. Therefore, we applied a linear scaling factor  $\zeta = 1.25$  in  $S'(\hbar\omega) = \zeta S(\hbar\omega)$  in all calculations of emission lineshapes to account for the underestimated atomic relaxations.

### S3 EMBEDDING METHODOLOGY

The embedding methodology described in Refs. [11, 36] was employed to model the vibrational properties of large supercells containing a defect. This approach exploits the short-range nature of interatomic forces in semiconductors to construct an effective Hessian matrix for systems containing thousands of atoms. The embedding scheme is illustrated in Fig. S1. When constructing the Hessian matrix elements, the following criteria are used:

- If two atoms lie within a specified cutoff radius  $r_b$ , the corresponding elements from the bulk supercell Hessian matrix are utilized.
- For atom pairs within a cutoff radius  $r_d$  from the defect, matrix elements from the defect-containing supercell are applied.
- In all other cases, the matrix elements are set to zero.

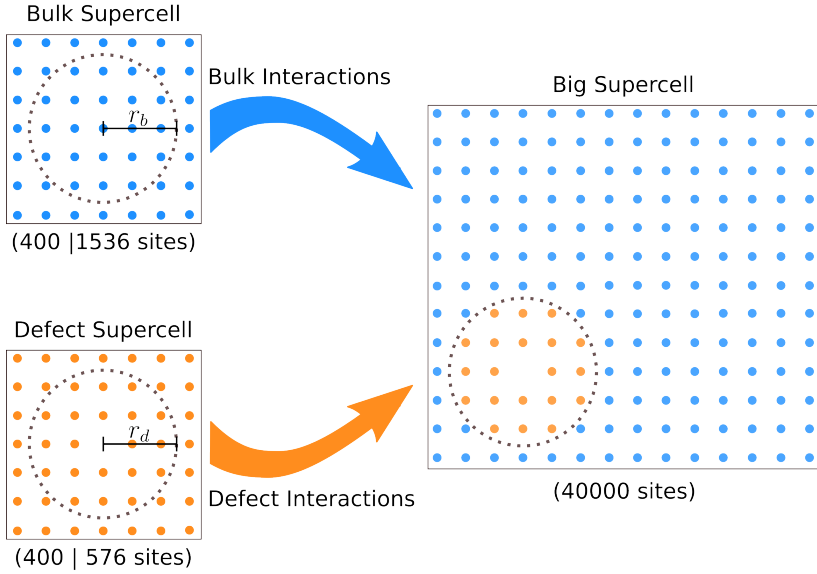


FIG. S1. Illustration of the embedding methodology for defect vibrational structure calculations.

For the zero strain case, we employed  $8 \times 8 \times 3$  bulk supercell with 1536 atomic sites and  $6 \times 6 \times 2$  defect supercells containing 576 atomic sites. The corresponding cutoff radii used in the embedding procedure were  $r_b = 12.200 \text{ \AA}$  and  $r_d = 9.228 \text{ \AA}$ . When a uniaxial strain of  $\pm 2\%$  was applied along the  $a$ -axis, smaller  $5 \times 5 \times 2$  bulk and defect supercells consisting of 400 atoms were used. For these strained supercells, the bulk cutoff radius was  $r_b = 7.000 \text{ \AA}$ , while the defect cutoff values were  $r_d = 7.690 \text{ \AA}$  for  $+2\%$  strain and  $r_d = 7.536 \text{ \AA}$  for  $-2\%$  strain.

The Hessian matrix was constructed from a  $25 \times 25 \times 8$  supercell containing 40 000 atomic sites. Using the embedding methodology, the vibrational basis is expanded from 1194 modes for the  $5 \times 5 \times 2$  supercell or 1722 modes for the  $6 \times 6 \times 2$  supercell to a total of 119994 vibrational modes, corresponding to an increase by a factor of up to  $\sim 100$  in the number of modes. This increase in the number of vibrational modes permits the use of smaller Gaussian smoothing widths  $\sigma$ , thereby yielding a higher spectral resolution. Such improved resolution is necessary for resolving fine features, for example the splitting of the first phonon sideband peak in the emission lineshape of  $V_{\text{Si}}^-(k)$ . As a further illustration, consider  $V_{\text{Si}}^-(h)$  under  $+2\%$  strain: the lowest vibrational mode obtained from a  $5 \times 5 \times 2$  supercell is 13.5 meV, whereas embedding into a  $25 \times 25 \times 8$  supercell reduces this value to 3.7 meV. Thus, the embedding methodology provides access to a substantially larger set of vibrational modes, including low-energy acoustic phonons, and a relaxation profile in the dilute limit [see Eq. S9].

#### S4 VIBRATIONAL STRUCTURES AND LOCALIZATION RATIOS

The vibrational properties of defects can be understood by examining the localization of its phonon modes [53]. Bulk-like modes are spatially extended and resemble plane-wave vibrations. In contrast, localized modes are confined to the vicinity of the defect and typically exhibit frequencies outside the host material's phonon band. Between these two cases lie the so-called quasi-local modes [36], which manifest as defect-induced vibrational resonances embedded within the continuum of bulk phonons. These resonances originate from a collection of vibrational states whose energies fall inside the bulk phonon spectrum. To provide a quantitative measure of phonon localization, we employ the inverse participation ratio (IPR). For a phonon mode  $k$ , the IPR is defined as [36, 53]

$$\text{IPR}_k = \frac{1}{\sum_m \boldsymbol{\eta}_{k;m}^4}, \quad (\text{S10})$$

where  $\boldsymbol{\eta}_{k;m}$  denotes the three-dimensional, normalized, mass-weighted displacement of atom  $m$  in mode  $k$ . Here,

$$\boldsymbol{\eta}_{k;m}^4 \equiv \left( \sum_{\alpha} \eta_{k;m\alpha}^2 \right)^2, \quad (\text{S11})$$

with  $\eta_{k;m\alpha}$  the mass-weighted displacement of atom  $m$  along Cartesian direction  $\alpha$ .

TABLE S2. Positions of prominent PSB peaks in the emission lineshape below the ZPL (in meV) for hexagonal and quasicubic configurations under  $\pm 2\%$  uniaxial strain along the  $a$ -axis. Vibrational mode types: BL – bulk-like, QL – quasi-local, QLR – quasi-local replica.

Strain	$V_{\text{Si}}^-(h)$			$V_{\text{Si}}^-(k)$				
	BL	QL	QLR	BL	QL	QLR		
0% (expt.)	37.2	74.0	76.4	147.9	36.2	42.0	76.0	151.5
0% (calc.)	38.5	74.8	76.6	149.6	38.2	43.3	75.8	151.1
+2%	37.3	44.5	74.0	147.8	38.8	43.9	74.2	147.6
-2%	38.8	76.8	78.2	153.2	39.1	43.7	77.4	154.2

The IPR provides an estimate of the number of atoms that participate significantly in a given vibrational mode:  $\text{IPR}_k = 1$  corresponds to a mode localized on a single atom, whereas  $\text{IPR}_k = N$  indicates that all  $N$  atoms in the supercell contribute equally. Intermediate cases, where only  $P < N$  atoms vibrate appreciably, yield  $\text{IPR}_k \approx P$ . Although the IPR offers a robust measure of localization, it is often more convenient to introduce the related localization ratio  $\beta_k$  [36], defined as

$$\beta_k = \frac{N}{\text{IPR}_k}. \quad (\text{S12})$$

Here larger values of  $\beta_k$  indicate stronger localization of phonon mode  $k$ , making this quantity particularly convenient when comparing defect-induced vibrational characteristics across different supercell sizes.

The top panels of Fig. S2 compare the computed bulk phonon density of states (DOS) of unstrained 4H-SiC (solid black line) with the experimental emission lineshapes (light gray) of the  $V_{\text{Si}}^-(h)$  and  $V_{\text{Si}}^-(k)$  defects. In the bottom panels the vertical gray lines are the calculated ground-state vibrational localization ratios  $\beta$ , obtained using a  $25 \times 25 \times 8$  supercell containing 40 000 atomic sites. These localization ratios allow us to identify which types of vibrational modes contribute to the phonon sideband (PSB). The calculated emission lineshapes show that the PSB of the  $V_{\text{Si}}^-$  defect in 4H-SiC comprises a mixture of bulk-like (BL), quasi-local (QL), and localized vibrational modes together with corresponding replicas (e.g. quasi-local replicas, QLR). The peak positions of most prominent PSB features are summarized in Table S2.

Fig. S3 illustrates how the bulk phonon DOS of 4H-SiC responds to uniaxial strain of 0%, -2%, and +2% along the  $a$ -axis. The bulk phonon DOS were obtained from  $8 \times 8 \times 3$  bulk supercells. Acoustic modes below 60 meV remain largely unchanged, whereas optical phonons in the 90–125 meV range exhibit a pronounced strain dependence: tensile strain (+2%, blue) “softens” these modes and shifts them to lower energies, while compressive strain (-2%, red) results in “hardening” and a corresponding upward shift.

Fig. S4 presents the vibrational structure of the  $V_{\text{Si}}^-(h)$  (left) and  $V_{\text{Si}}^-(k)$  (right) configurations under the same strain conditions. Each panel includes the strain-dependent bulk phonon DOS (solid lines) and localization ratios  $\beta$  (vertical bars) for each vibrational mode of the negatively charged ground state, computed using a  $25 \times 25 \times 8$  supercell (40 000 atomic sites). The overlaid DOS highlights the influence of host crystal vibrational modes how their energies shift under strain.

## S5 EXPERIMENTAL SETUP

We employ transient absorption (TA) spectroscopy to measure the stimulated emission spectrum of the  $V_{\text{Si}}^-(h)$  and  $V_{\text{Si}}^-(k)$  cases. We selectively pump at the  $V_{\text{Si}}^-(h)$  and  $V_{\text{Si}}^-(k)$  ZPLs with a sub-5  $\text{cm}^{-1}$  ( $\sim 0.6$  meV) narrow-band optical parametric oscillator (OPO) laser (EKSPLA NT242), which allows us to pump the sample anywhere in the 210-2600 nm (0.48-5.9 eV) spectral range. A probe pulse then arrives at the sample about 4 ns later. The measured quantity is the change of the transmission ( $\Delta T/T$ ) of the probe with and without the presence of the pump. The signal attributed to the stimulated emission is the increase in the transmission of the probe ( $\Delta T/T > 0$ ) on the red side (lower energy) of the spectrum with respect to the ZPL. This is not to be confused with the ground state bleaching (or absorption spectrum), which also results in  $\Delta T/T > 0$ , but in the blue side (higher energy) of the TA spectrum with respect to the ZPL. In fact, at the ZPL, the signal contains contribution from both the stimulated emission and absorption sides. Combined with the fact that pump scattering for resonant excitation also invalidates the TA spectrum at the ZPL, the stimulated emission spectrum is omitted at this particular spectral position. The TA spectroscopy setup has already been employed in several previous publications [38, 39, 54]. All measurements were performed at sub-10 K temperature.

An advantage of the method employed is the precise pumping of the ZPLs: this allows us to obtain an emission spectrum only from the  $V_{\text{Si}}^-(k)$  configuration by pumping resonantly at the ZPL (916 nm/1.353 eV). This is in contrast

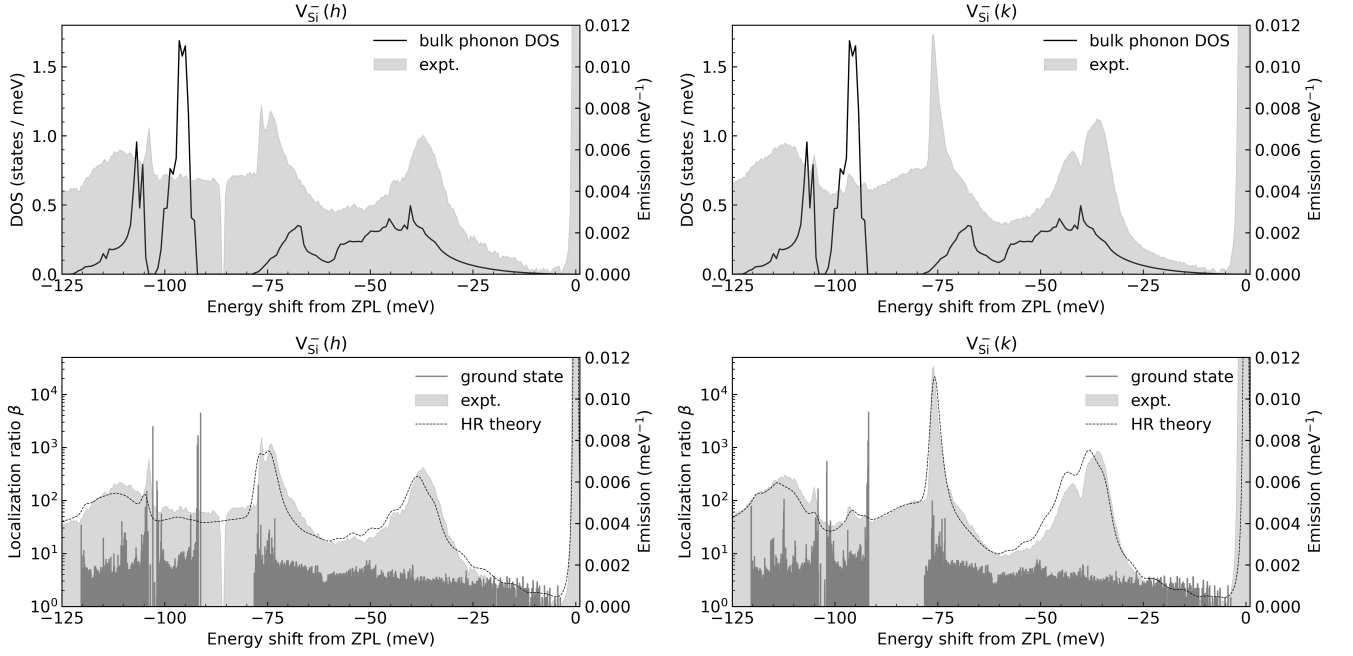


FIG. S2. Comparison of vibrational and optical properties of the  $V_{\text{Si}}^-(h)$  and  $V_{\text{Si}}^-(k)$  defects in unstrained 4H-SiC. Shaded areas in light-gray color are experimental emission lineshapes while dashed gray lines are emission lineshapes calculated using HR theory. The solid black line shows the calculated bulk phonon density of states (DOS). Vertical gray lines show the ground-state vibrational localization ratios  $\beta$  computed for a  $25 \times 25 \times 8$  supercell (40 000 atomic sites).

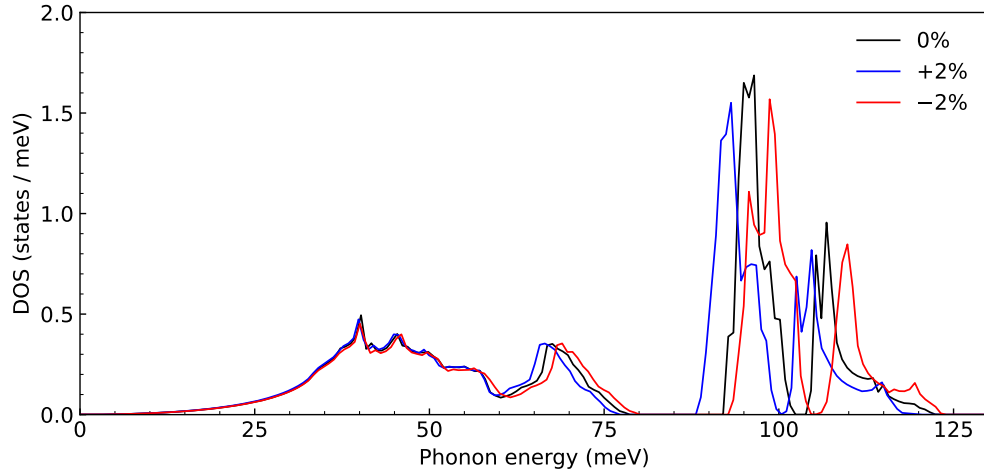


FIG. S3. Calculated density of states (DOS) of phonons in pure 4H-SiC at 0% (in black), +2% (in blue), and -2% (in red) strain along  $a$ -axis.

to a few previous works where the excitation wavelength is fixed (at 730 nm (1.70 eV) [22] or 808 nm [49]). However, as the sample studied in this work is in bulk, it contains both  $V_{\text{Si}}^-(h)$  and  $V_{\text{Si}}^-(k)$  configurations. Since the ZPL of the  $V_{\text{Si}}^-(k)$  case is lower in energy compared to the  $V_{\text{Si}}^-(h)$  configuration (at 861 nm/1.439 eV), the stimulated emission spectrum of the  $V_{\text{Si}}^-(k)$  case is without the contribution of the  $V_{\text{Si}}^-(h)$ . However, the  $V_{\text{Si}}^-(h)$  would contain a small contribution of the  $V_{\text{Si}}^-(k)$  as the pump also has enough photon energy to excite the  $V_{\text{Si}}^-(k)$  configuration. This contribution is substantial at the ZPL of  $V_{\text{Si}}^-(k)$  and is removed from the spectrum of the  $V_{\text{Si}}^-(h)$  defect. The ZPL of  $V_{\text{Si}}^-(k)$  lies 86 meV below the ZPL of  $V_{\text{Si}}^-(h)$ . This ZPL difference falls in the phonon gap (see Fig. S2) and does not overlap with vibrational features in emission spectra of  $V_{\text{Si}}^-(h)$  validating the  $V_{\text{Si}}^-$  ensemble measurements of

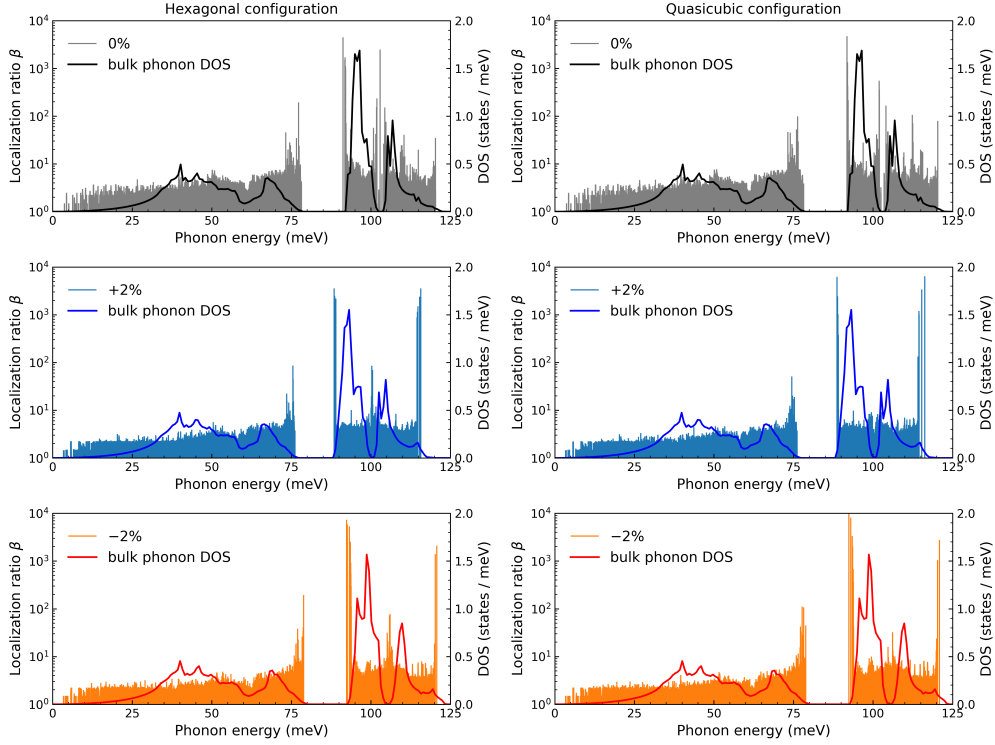


FIG. S4. Vibrational structures of the  $V_{\text{Si}}^-(h)$  (left side) and  $V_{\text{Si}}^-(k)$  (right side) defects at 0%, +2%, and -2% strain along  $a$ -axis, respectively. Vertical lines correspond to localization ratios  $\beta$  of vibrational modes of the  $25 \times 25 \times 8$  supercell (40 000 atomic sites) of the ground state. The solid line corresponds to the density of states (DOS) of phonons in pure 4H-SiC at 0% (black line), +2% (blue line), and -2% (red line) strain along  $a$ -axis.

stimulated emission.

A comparison between experimental emission lineshapes reported in Refs. [22, 49] and those obtained in this work is shown in Fig. S5. For the  $V_{\text{Si}}^-(h)$  center, the PSB is more clearly resolved in this work, revealing a distinct double-peak structure associated with quasi-local vibrational modes located at 74.0 and 76.4 meV below the ZPL. In addition, a localized defect vibrational mode at 103.8 meV below the ZPL is clearly resolved. For the  $V_{\text{Si}}^-(k)$  center, the emission lineshape obtained in this work more clearly reveals localized vibrational modes at 92.8 and 105.0 meV below the ZPL, as well as a vibrational resonance at 96.5 meV below the ZPL.

### S5.A Oblique Incidence Probe Configuration

Under the  $C_{3v}$  point group, the transition dipole moments transform as either  $(x, y)$  ( $E$ ) or  $z$  ( $A_1$ ) in Cartesian coordinates. For example, optical transitions between electronic states  $A_2 \leftrightarrow A_2$  (whose direct product transforms as  $A_1$ ) is allowed by  $z$  dipoles, while the  $A_2 \leftrightarrow E$  transition (direct product transforms as  $E$ ) is allowed with  $x, y$  dipoles [22].

We can summarize this experimental scheme with a few useful statements:

- 0°-polarization probe can observe all transitions in either  $V_{\text{Si}}^-(h)$  or  $V_{\text{Si}}^-(k)$  configuration.
- 90°-polarization probe only couples to the  $\mu_y$  dipole, thus any transition allowed by  $\mu_z$  cannot be observed by the probe pulse.

To achieve oblique incidence, a  $c$ -cut 4H-SiC sample was placed at an angle of  $45^\circ$  with the incident beam. However, due to the considerable refractive index mismatch between the SiC sample and vacuum (approximately 2.7 and 1, respectively), the beam enters the sample at a much smaller angle ( $\sim 15^\circ$ ), therefore barely probing the  $\mu_z$  component. To resolve this issue, the sample was positioned between two high refractive index rutile right-angle prisms, thereby ensuring the beam passed with minimal refraction (see Fig. S6 for a schematic representation of the

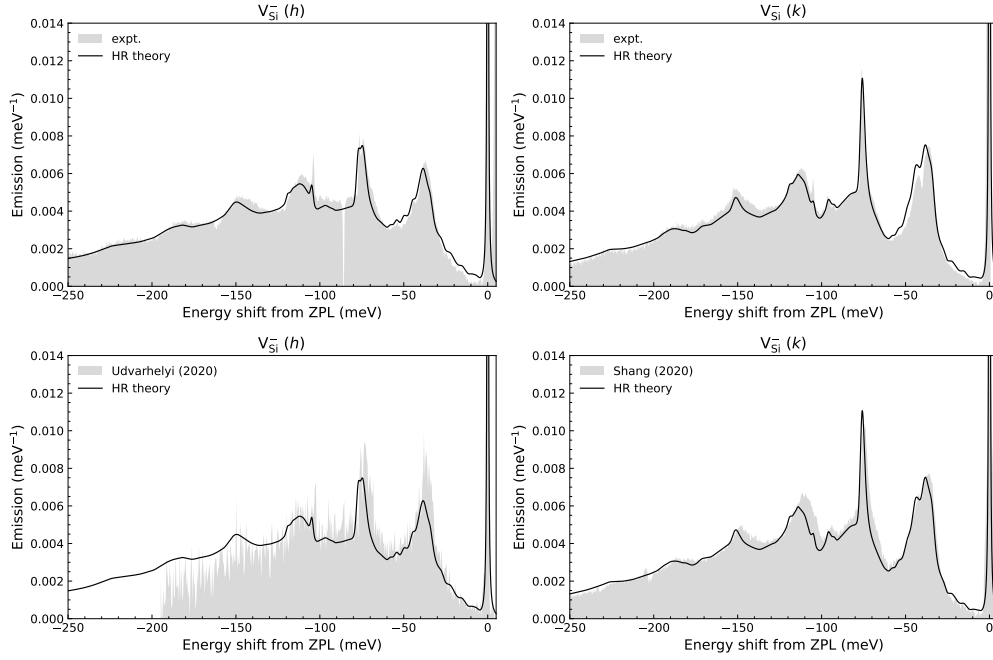


FIG. S5. Calculated emission lineshapes for supercells with  $V_{\text{Si}}^-(h)$  and  $V_{\text{Si}}^-(k)$  defects at zero strain. Lineshapes were computed with  $r^2\text{SCAN}$  functional using HR theory and extrapolated to the dilute limit, approximated by a  $25 \times 25 \times 8$  supercell with 40 000 atomic sites. Experimental spectra from this work and Refs. [22, 49].

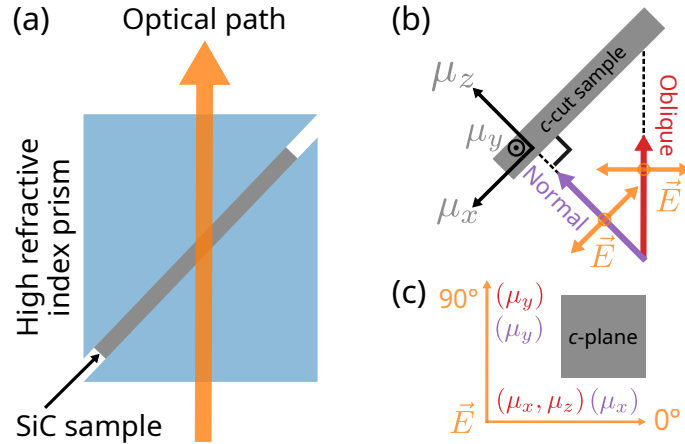


FIG. S6. (a) Schematic illustration of the 4H-SiC sample sandwiched between two high refractive index rutile prisms, together with the optical path. (b) Top view schematic of probing geometry for normal (in purple) and oblique (in red) incidence cases of  $V_{\text{Si}}^-$  electronic transitions with respect to the  $c$ -plane. The coordinate system defining the transition dipole moments  $\mu_x$ ,  $\mu_y$  and  $\mu_z$ , is indicated. Orange arrows denote the electric field vectors  $\vec{E}$  of the probe beam. (c) Front view schematic of the sample ( $c$ -plane) in the laser beam direction, with summary of the transition dipole moments excited by the  $0^\circ$  or  $90^\circ$  polarization of the electric field vector.

sample configuration). Although passing the laser pulses through the prisms chirps the pulses to a few ps and limits the temporal resolution, the spectra presented here are obtained at a pump-probe delay of about 4 ns.